Frequency-constrained Unit Commitment Considering Coordinated Frequency Control Strategy of Wind Turbines and Energy Storage System

Hwang Goh Hui, *Senior Member*, *IEEE*, Yuxin Ou, Wei Dai, *Member*, *IEEE*, Hui Liu, *Senior Member*, *IEEE*, Tonni Agustiono Kurniawan, and Jun Xu

***Abstract*—To maintain the frequency stability of power systems integrated with large-scale renewable energy sources (RESs), a frequency-constrained unit commitment (FCUC) model is proposed, which incorporates a coordinated frequency control strategy of wind turbines and energy storage system (WT-ESS), a vital component for enhancing frequency regulation capacity of wind farms. Analytical formulations for the maximum rate of change of frequency (RoCoF) and steady-state frequency deviation are derived for both serial control and parallel control, accounting for the output-limited state of energy storage under serial control. To address the problem of solution slowness caused by the strong nonlinear frequency nadir constraints, a model-based multi-directional bilayer solution method is proposed. This method employs the simulation model to detect whether the frequency nadir constraint is active and generates parallel optimized cuts in three directions. Simulation results on the IEEE 39-bus test system demonstrate that the proposed FCUC model and solution method could accurately reflect the primary frequency regulation (PFR) characteristics of WT-ESS. Furthermore, the coordinated frequency control strategy effectively reduces overall operating costs while ensuring frequency security.**

***Index Terms*—Renewable energy source, frequency stability, frequency-constrained unit commitment, wind turbine, energy storage system, primary frequency regulation.**

I. Introduction

THE increased deployment of large-scale renewable energy sources (RESs) in power systems brings challenges to ensuring system stability [1], [2], notably in maintaining frequency security [3], [4]. Different from synchronous generators, RESs connected via power electronic converters lack the physical inertia to stabilize the system frequency [5], [6]. This reduction in inertia and primary frequency regulation (PFR) capabilities jeopardizes system safety. To mitigate this issue, the frequency constraints can be incorporated into the unit commitment model. Current research on frequency-constrained unit commitment (FCUC) focuses on two critical areas: expanding PFR resource utilization and addressing nonlinear frequency constraints.

Reference [7] integrated frequency constraints into unit commitment to ensure PFR adequacy but overlooked dynamic frequency changes. Building on this, [8] examined the impact of grid-connected wind power capacity on PFR by incorporating wake effects into the FCUC model. Reference [9] developed a frequency response model for systems with multiple RESs, while [10] and [11] assessed PFR capabilities of wind turbines (WTs) and energy storage system (ESS) separately. However, the coordinated involvement of RESs and ESS in PFR within FCUC was not considered.

Advancements in power electronics and frequency regulation control offer RESs and ESS new opportunities to provide PFR capability [12]. Techniques such as overspeed load shedding, pitch control, rotor deceleration control, virtual inertia control, and droop control enhance the frequency support of WTs. However, the PFR capacity of WTs is limited by rotor speed and slow pitch control response, posing challenges in meeting PFR demands. ESS has fast response speed and can operate stably. Utilizing ESS to assist WTs can improve the PFR capability of WTs, thereby enhancing the overall PFR capability of WT-ESS [13], [14]. Numerous studies have examined the control strategies employed by WT-ESS in providing frequency support. One perspective is that the ESS serves to provide the energy supply when and where necessary, depending on whether the rotor speed of WT reaches its minimum permitted speed [15], [16]. Some studies treat WT and ESS in an identical manner, whereby the allocation of PFR power is contingent upon the power margin of each unit [17]. Some studies have proposed the concept of utilizing the WT to absorb as much continuous power as feasible, with the ESS assuming the responsibility

Manuscript received: September 2, 2024; revised: December 31, 2024; accepted: April 14, 2025. Date of CrossCheck: April 14, 2025. Date of online publication: April 22, 2025.

This work was supported in part by the National Natural Science Foundation of China (No. 52107082) and in part by Major Talents Program of Guangxi of China.

H. H. Goh, Y. Ou, W. Dai (corresponding author), H. Liu, T. A. Kurniawan, and J. Xu are with the Guangxi Key Laboratory of Power System Optimization and Energy Technology, Guangxi University, Nanning 530004, China (e-mail: hhgoh@gxu.edu.cn; 302741216@qq.com; wei-dai2019@163.com; hughlh@gxu.edu.cn; tonni696390@gmail.com; xujun980720@163.com).

DOI: 10.35833/MPCE.2024.000976

of rectifying any deficiencies in the power supply [18]. However, after considering the control strategy of WT-ESS, the impact of their PFR task allocation on system operation scheduling has not been considered. This paper addresses this gap by proposing an FCUC model that considers coordinated frequency control strategies of WT-ESS.

For nonlinear frequency constraints, existing studies have predominantly employed an analytical approach to incorporate highly nonlinear frequency response indices into FCUC models [19]. This approach involves simplifying component models and neglecting power flow to construct low-dimensional system frequency regulation (SFR) models. Reference [20] introduced a low-order SFR model capturing fundamental system dynamics, albeit limited to reheat steam generators. Reference [21] aggregated multi-machine SFR models into single-machine representations, utilized by [11] and [22] to derive time-domain expressions for frequency nadir. Furthermore, they integrated linearized frequency constraints into conventional unit commitment. Reference [23] introduced an open-loop linear model accommodating various unit types, later extended by [19] with parabolic frequency deviation and polynomial fit to capture PFR. On this basis, [24] proposed a processing method for frequency nadir constraint based on estimating the maximum perturbation the system can withstand. References [25]-[27] simplified turbine and inverter time constants to derive time-domain frequency expressions and linearize frequency nadir constraints. Reference [28] utilized Benders decomposition to solve the mixed-integer linear programming (MICP) problem for microgrid frequency stability and cost optimization. However, these methods are unable to effectively handle the nonlinearities arising from the intermixing of PFR resources within the system. Reference [29] employed block diagram modeling tools to capture dynamic frequency processes and nonlinear features. However, their complex setups result in long simulation time, which is not suitable for FCUC models. In contrast, the simulation time can be reduced by using the low-order transfer function, which makes it suitable for its inclusion in the FCUC model.

So far, the current FCUC models neglect the influence of frequency control strategies of WT-ESS on PFR performance. Moreover, the nonlinear nature of the SFR model, particularly with coordinated frequency control, poses a challenge to existing analytical methods. In comparison with the existing results, this paper considers the role of frequency control strategies of WT-ESS in the FCUC model, providing an accurate analysis of the effects of different control strategies on the frequency response indices. Additionally, a model-based multi-directional bilayer solution method is proposed to solve the highly nonlinear frequency nadir constraints after embedded frequency control strategies, which are difficult to handle by existing methods.

1) A system frequency response model for the WT-ESS under the serial and parallel control is proposed to obtain the frequency response indices. The expressions of the frequency response indices under the serial control and parallel control are derived.

2) An enhanced FCUC model is developed by combining the frequency control strategies of the WT-ESS. The derived frequency constraints under the serial control and parallel control are incorporated into the construction of the FCUC model. This model allows flexibly adjusting control strategies to optimize PFR capacity to meet the frequency requirements.

3) A model-based multi-directional bilayer solution method is proposed to address the highly nonlinear frequency nadir constraint resulting from frequency control strategies of WT-ESS. The inner and outer layers are connected through optimized cuts.

The remainder of this paper is organized as follows. Section II constructs the system frequency response models with the quantitative expressions of the PFR capabilities of the system. Section III builds the FCUC model considering coordinated frequency control strategy of WT-ESS. Section IV describes the proposed model-based multi-directional bilayer solution method. Section V presents the case studies. Finally, conclusions are drawn in Section VI.

II. System Frequency Response Models

This section focuses on constructing dynamic frequency response models for thermal power unit (TPU) and WT-ESS under the serial control and parallel control. Furthermore, based on these response models, a method for calculating the dynamic frequency response indices is proposed.

A. Frequency Response Model of TPU

During the steady-state operation, the mechanical torque, electromagnetic torque, friction torque, and wind resistance are balanced to maintain rotor speed. However, when the system frequency exceeds the PFR dead zone, the torque balance is disrupted, as described by the rotor motion equation:

$$2H_{\mathrm{G}}\frac{\mathrm{d}\Delta f}{\mathrm{d}t}+D_{\mathrm{G}}\Delta f=\Delta P_{\mathrm{G}}-\Delta P_{\mathrm{G,E}} \tag{1}$$

where Δf is the frequency deviation; and ΔP_{G}, $\Delta P_{\mathrm{G,E}}$, H_{G}, and D_{G} are the mechanical power variation, electromagnetic power variation, inertia time constant, and damping constants of the generator, respectively.

In modern TPU, intermediate reheat turbines are used. The transfer function of TPU [25] can be expressed as:

$$\Delta P_{\mathrm{G}}(s)=-\frac{K_{\mathrm{G}}^{\mathrm{P}}+K_{\mathrm{G}}^{\mathrm{I}}/s}{1+R(K_{\mathrm{G}}^{\mathrm{P}}+K_{\mathrm{G}}^{\mathrm{I}}/s)}\Delta f(s) \tag{2}$$

where R is the adjustment coefficient of TPU; and $K_{\mathrm{G}}^{\mathrm{P}}$ and $K_{\mathrm{G}}^{\mathrm{I}}$ are the proportional and integral coefficients for the frequency response model of TPU, respectively.

B. Frequency Response Model of WT-ESS

WTs typically utilize virtual synchronous generator (VSG) technology to provide virtual inertia control and droop control through overspeed load-shedding mode and pitch angle control mode, respectively. The transfer functions of virtual inertia control $G_{\mathrm{w,i}}(s)$ and droop control $G_{\mathrm{w,d}}(s)$ can be expressed as (3) and (4), respectively.

$$G_{\mathrm{w,i}}(s)=\frac{\Delta P_{\mathrm{w,i}}(s)}{\Delta f(s)}=-\frac{k_{\mathrm{i}}s}{1+T_{\mathrm{w,i}}s} \tag{3}$$

$$G_{\mathrm{w,d}}(s)=\frac{\Delta P_{\mathrm{w,d}}(s)}{\Delta f(s)}=-\frac{k_{\mathrm{d}}}{1+T_{\mathrm{w,d}}s} \tag{4}$$

where $\Delta P_{\mathrm{w,i}}$ and $\Delta P_{\mathrm{w,d}}$ are the frequency response power under virtual inertia control and droop control for WTs, respectively; k_{i} is the virtual inertia control coefficient; k_{d} is the droop control coefficient; $T_{\mathrm{w,i}}$ is the response time constant for virtual inertial control of WTs; and $T_{\mathrm{w,d}}$ is the response time constant for droop control of WTs.

WTs with ESS can be used as PFR resources of power system to solve the problems of insufficient output and slow response of WTs in PFR process. Similar to WTs, ESS can participate in PFR through virtual inertia control and droop control. Since ESS is integrated with the wind farm, the virtual inertia control and droop control coefficients of ESS participating in PFR are identical to those of WTs. The PFR transfer function of ESS can be expressed as:

$$G_{\mathrm{E}}(s)=\frac{\Delta P_{\mathrm{E}}(s)}{\Delta f(s)}=-\frac{k_{\mathrm{i}}s+k_{\mathrm{d}}}{1+T_{\mathrm{E}}s} \tag{5}$$

where ΔP_{E} is the frequency response power of ESS; and T_{E} is the response time constant of ESS.

C. SFR Model Incorporating Frequency Control Strategies of WT-ESS

The uniform system consists of TPUs and converter-based WT-ESS, whose SFR model is depicted in Fig. 1, where N_{G} is the number of TPUs, indexed by i; B_i^{G} is the state of TPU i, which equals 1 when TPU i is on and 0 when it is off; $P_{\mathrm{N},i}^{\mathrm{G}}$ is the rated power of TPU i; $\Delta P_{\mathrm{WT\text{-}ESS}}$ is the frequency response power of WT-ESS; ΔP_{L} is the PFR response power variation of system loads; k_{L} is the frequency adjustment coefficient of loads; P_{Ln} is the load when the system frequency is kept at its rated value; and ΔP_{LW} is the total disturbance endured by the system, which is calculated as:

$$\Delta P_{\mathrm{LW}}=\Delta P_{\mathrm{Le}}-\Delta P_{\mathrm{We}} \tag{6}$$

where ΔP_{Le} is the amount of load disturbance; and ΔP_{We} is the amount of wind power disturbance.

The frequency control strategy of the WT-ESS is categorized based on the specific task allocation of the ESS and WTs in response to PFR commands [14]. Two SFR models are developed for the WT-ESS: one employing serial control and the other employing parallel control.

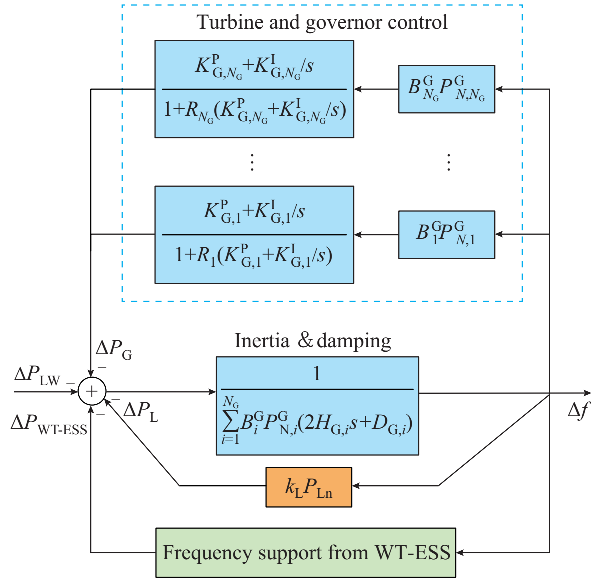

Fig. 1. SFR model of uniform system.

1) Serial Control of WT-ESS

Under the serial control, the WTs initially respond to the PFR command from the power system. At this stage, the WTs adjust the power output autonomously using virtual inertia control and droop control to participate in PFR. If the output of WTs is insufficient, the ESS will step in to complete the remaining PFR tasks, ensuring the fulfillment of PFR requirements. The ESS output is minimal, as it only addresses uncompleted PFR tasks of WTs. This serial control reduces the reserve demand of the ESS and preserves reserve capacity for future PFR tasks. Figure 2 illustrates the serial control of WT-ESS, where $P_{k,\max}^{\mathrm{B}}$ is the maximum power of ESS k; P_k^{forecast} is the forecasted power of wind farm k; and ΔP_{W} is the frequency response power of wind farms.

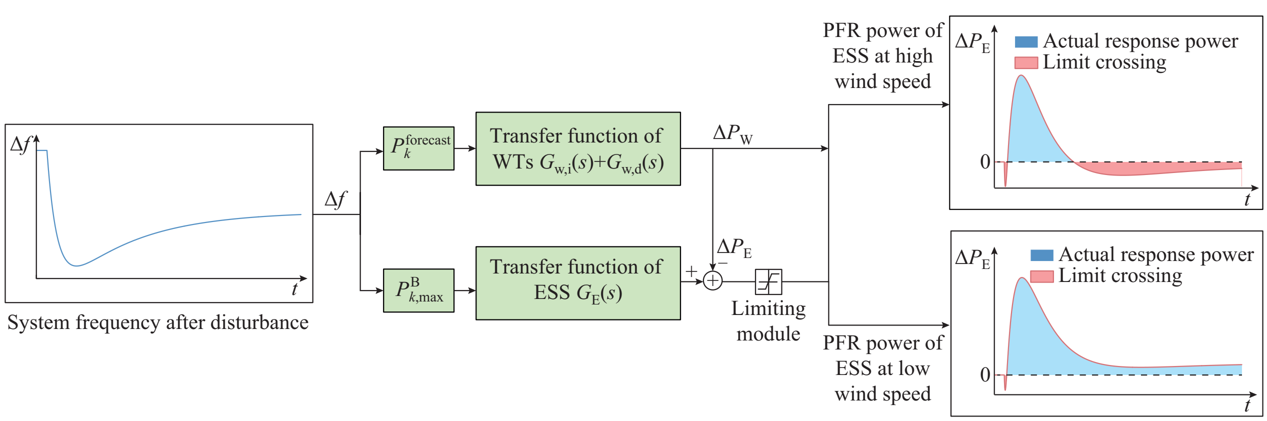

Fig. 2. Serial control of WT-ESS.

Under the serial control, the PFR capacity of ESS depends on the real-time generation of its corresponding WTs. When the response power of ESS exceeds its limit, it is managed by the highly nonlinear limiting module. To accurately assess the impact of the serial control, it is crucial to comprehensively consider the role of the limiting module in frequency response analysis.

The transfer function of the uniform system shown in Fig. 1 can be expressed as:

$$\frac{\Delta f}{\Delta P_{\mathrm{LW}}} = -\left\{\sum_{i=1}^{N_{\mathrm{G}}} B_{i,t}^{\mathrm{G}} P_{\mathrm{N},i}^{\mathrm{G}} (2H_{\mathrm{G},i}s + D_{\mathrm{G},i}) + \sum_{k=1}^{N_{\mathrm{WE}}} [\max(0, P_{k,\max}^{\mathrm{B}} G_{\mathrm{E}}(s) - B_{k,t}^{\mathrm{WE,s}} P_{k,t}^{\mathrm{forecast}}(G_{\mathrm{w,i}}(s)+G_{\mathrm{w,d}}(s)))] + \sum_{k=1}^{N_{\mathrm{WE}}} P_{k,t}^{\mathrm{forecast}}(G_{\mathrm{w,i}}(s)+G_{\mathrm{w,d}}(s)) + \sum_{i=1}^{N_{\mathrm{G}}} B_{i,t}^{\mathrm{G}} P_{\mathrm{N},i}^{\mathrm{G}} \frac{K_{\mathrm{G},i}^{\mathrm{P}} + K_{\mathrm{G},i}^{\mathrm{I}}/s}{1+R_i(K_{\mathrm{G},i}^{\mathrm{P}}+K_{\mathrm{G},i}^{\mathrm{I}}/s)} + k_{\mathrm{L}} P_{\mathrm{Ln},t}\right\}^{-1} \tag{7}$$

where $B_{k,t}^{\mathrm{WE,s}}$ represents the control strategy used by WT-ESS at time t, which equals 1 and 0 when serial control and parallel control are adopted, respectively; and N_{WE} is the number of WT-ESS. The response of the TPU governor is approximately twenty times faster than that of damping. Thus, $D_{\mathrm{G},i}$ in (7) is set to be 0 [19].

The calculation of the steady-state frequency deviation value must account for the effect of the limiting module in serial control and the predicted power of wind farm on ESS response. The steady-state frequency deviation can be obtained by substituting $B_{k,t}^{\mathrm{WE,s}}=1$ and $s=0$ into (7) since the rates of change are all 0 in the steady state. Therefore, the expression for the steady-state frequency deviation $\Delta f_{\mathrm{ss},t}^{*}$ is derived as:

$$\Delta f_{\mathrm{ss},t}^{*} = -\frac{\Delta P_{\mathrm{LW}}}{\sum_{k=1}^{N_{\mathrm{WE}}} \max(0, P_{k,\max}^{\mathrm{B}} k_{\mathrm{d}} - P_{k,t}^{\mathrm{forecast}} k_{\mathrm{d}}) + \sum_{i=1}^{N_{\mathrm{G}}} \frac{B_{i,t}^{\mathrm{G}} P_{\mathrm{N},i}^{\mathrm{G}}}{R_i} + \sum_{k=1}^{N_{\mathrm{WE}}} P_{k,t}^{\mathrm{forecast}} k_{\mathrm{d}} + k_{\mathrm{L}} P_{\mathrm{Ln},t}} \tag{8}$$

where the superscript * indicates the per-unit value.

The maximum rate of change of frequency (RoCoF) $RoCoF_{\max,t}^{*}$ is primarily linked to the system overall inertia and determined using (9):

$$RoCoF_{\max,t}^{*} = \frac{\Delta P_{\mathrm{LW}}}{2\sum_{i=1}^{N_{\mathrm{G}}} B_{i,t}^{\mathrm{G}} P_{\mathrm{N},i}^{\mathrm{G}} H_{\mathrm{G},i}} \tag{9}$$

2) Parallel Control of WT-ESS

Under the parallel control, WTs and ESS respond to the PFR commands of power system according to their respective tasks.

This control treats the ESS as an independent PFR reserve resource. The output power of ESS decreases as other conventional PFR resources increase. However, during the PFR response period, the ESS continues to output power throughout the cycle until the PFR task is completed to maintain system stability. This parallel control can elevate the frequency nadir of the system by offering more energy support in the early stages of the disturbance. Figure 3 illustrates the parallel control of WT-ESS.

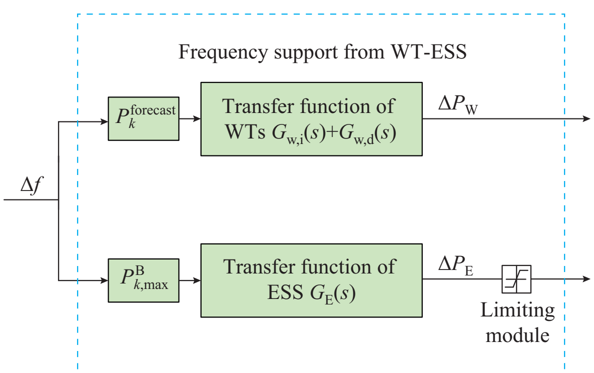

Fig. 3. Parallel control of WT-ESS.

Similar to (8), the expression for the steady-state frequency deviation under the parallel control can be derived by substituting $B_{k,t}^{\mathrm{WE,s}}=0$ and $s=0$ into (7):

$$\Delta f_{\mathrm{ss},t}^{*} = -\frac{\Delta P_{\mathrm{LW}}}{\sum_{k=1}^{N_{\mathrm{WE}}} P_{k,\max}^{\mathrm{B}} k_{\mathrm{d}} + \sum_{i=1}^{N_{\mathrm{G}}} \frac{B_{i,t}^{\mathrm{G}} P_{\mathrm{N},i}^{\mathrm{G}}}{R_i} + \sum_{k=1}^{N_{\mathrm{WE}}} P_{k,t}^{\mathrm{forecast}} k_{\mathrm{d}} + k_{\mathrm{L}} P_{\mathrm{Ln},t}} \tag{10}$$

Utilizing the aforementioned indices, both serial control and parallel control of WT-ESS can be coordinated into the construction of the FCUC model.

III. FCUC Model Considering Coordinated Frequency Control Strategy of WT-ESS

A. Objective Function

The objective of the FCUC model is to minimize the operating cost while ensuring system safety. To maximize the utilization of wind power, it is treated as a resource with zero generation cost. The objective function is represented by:

$$C_{\min} = C_{\mathrm{G,run}} + C_{\mathrm{G,re}} + C_{\mathrm{G,start}} + C_{\mathrm{W,abandon}} + C_{\mathrm{B,re}} \tag{11}$$

where $C_{\mathrm{G,run}}$, $C_{\mathrm{G,re}}$, and $C_{\mathrm{G,start}}$ are the operating cost, PFR reserve cost, and start-up cost of TPU, respectively; $C_{\mathrm{W,abandon}}$ is the cost of wind abandonment penalties for wind farms; and $C_{\mathrm{B,re}}$ is the PFR reserve cost of ESS. The calculation of each cost is outlined below:

$$C_{\mathrm{G,run}} = \sum_{t=1}^{T}\sum_{i=1}^{N_{\mathrm{G}}} (a_i P_{i,t}^{\mathrm{G}} + b_i B_{i,t}^{\mathrm{G}}) \tag{12}$$

$$C_{\mathrm{G,re}} = \sum_{t=1}^{T}\sum_{i=1}^{N_{\mathrm{G}}} c_i R_{i,t}^{\mathrm{G}} \tag{13}$$

$$C_{\mathrm{G,start}} = \sum_{t=1}^{T}\sum_{i=1}^{N_{\mathrm{G}}} d_i B_{i,t}^{\mathrm{G}} (1 - B_{i,t-1}^{\mathrm{G}}) \tag{14}$$

$$C_{\mathrm{W,abandon}} = \sum_{t=1}^{T}\sum_{k=1}^{N_{\mathrm{WE}}} C^{\mathrm{W}} (P_{k,t}^{\mathrm{forecast}} - P_{k,t}^{\mathrm{W}} - R_{k,t}^{\mathrm{W}}) \tag{15}$$

$$C_{\mathrm{B,re}} = \sum_{t=1}^{T}\sum_{k=1}^{N_{\mathrm{WE}}} C^{\mathrm{B}} R_{k,t}^{\mathrm{B}} \tag{16}$$

where a_i and b_i are the power purchase cost coefficients for

TPU i; c_i and d_i are the reserve cost factor and start-up cost factor for TPU i, respectively; $P_{i,t}^{\mathrm{G}}$ is the output power of TPU i at time t; $R_{i,t}^{\mathrm{G}}$ is the PFR reserve capacity of TPU i at time t; C^{W} is the wind abandonment cost factor; $P_{k,t}^{\mathrm{W}}$ is the output power of wind farm k at time t; $R_{k,t}^{\mathrm{W}}$ is the PFR reserve capacity of wind farm k at time t; $R_{k,t}^{\mathrm{B}}$ is the PFR reserve capacity of ESS k at time t; C^{B} is the reserve cost factor of ESS; and T is the number of time periods indexed by t.

B. Constraints

The constraints of FCUC model involve constraints of TPU, operational constraints of power system, operational constraints of wind farm, and operational constraints of ESS.

1) Constraints of TPU

The constraints of TPU encompass unit output constraint (17), on/off time constraints (18), ramp-up constraints (19), and PFR reserve constraints (20).

$$B_{i,t}^{\mathrm{G}} P_{i,\min}^{\mathrm{G}} \le P_{i,t}^{\mathrm{G}} \le B_{i,t}^{\mathrm{G}} P_{i,\max}^{\mathrm{G}} \tag{17}$$

$$\begin{cases} T_{i,t}^{\mathrm{ON}} - (B_{i,t-1}^{\mathrm{G}} - B_{i,t}^{\mathrm{G}}) T_i^{\mathrm{ON,min}} \ge 0 \\ T_{i,t}^{\mathrm{OFF}} - (B_{i,t}^{\mathrm{G}} - B_{i,t-1}^{\mathrm{G}}) T_i^{\mathrm{OFF,min}} \ge 0 \end{cases} \tag{18}$$

$$\begin{cases} P_{i,t}^{\mathrm{G}} - P_{i,t-1}^{\mathrm{G}} \le R_i^{\mathrm{UP}} B_{i,t-1}^{\mathrm{G}} + P_{i,\min}^{\mathrm{G}} (B_{i,t}^{\mathrm{G}} - B_{i,t-1}^{\mathrm{G}}) \\ P_{i,t-1}^{\mathrm{G}} - P_{i,t}^{\mathrm{G}} \le R_i^{\mathrm{DN}} B_{i,t}^{\mathrm{G}} + P_{i,\min}^{\mathrm{G}} (B_{i,t-1}^{\mathrm{G}} - B_{i,t}^{\mathrm{G}}) \end{cases} \tag{19}$$

$$\begin{cases} P_{i,t,\max}^{\mathrm{G,L}} = \dfrac{B_{i,t}^{\mathrm{G}} P_{\mathrm{N},i}^{\mathrm{G}}}{R_i} (-\Delta f_{\mathrm{ss}}^*) \\ P_{i,t}^{\mathrm{G}} + P_{i,t,\max}^{\mathrm{G,L}} \le B_{i,t}^{\mathrm{G}} P_{i,\max}^{\mathrm{G}} \\ P_{i,t}^{\mathrm{G}} - P_{i,t,\max}^{\mathrm{G,L}} \ge B_{i,t}^{\mathrm{G}} P_{i,\min}^{\mathrm{G}} \\ R_{i,t}^{\mathrm{G}} \ge P_{i,t,\max}^{\mathrm{G,L}} \end{cases} \tag{20}$$

where $P_{i,\min}^{\mathrm{G}}$ and $P_{i,\max}^{\mathrm{G}}$ are the minimum and maximum output power of TPU i, respectively; $T_i^{\mathrm{ON,min}}$ and $T_i^{\mathrm{OFF,min}}$ are the minimum continuous on-time and off-time of TPU i, respectively; $T_{i,t}^{\mathrm{ON}}$ and $T_{i,t}^{\mathrm{OFF}}$ are the time when TPU i has been continuously on and continuously off at time t, respectively; R_i^{UP} and R_i^{DN} are the maximum ramp-up and ramp-down limits of TPU i, respectively; and $P_{i,t,\max}^{\mathrm{G,L}}$ is the amount of steady-state PFR power change of TPU i at time t.

2) Operational Constraints of Power System

The operational constraints of power system include power balance constraint (21), line security constraint (22), and system PFR reserve constraint (23).

$$\sum_{i=1}^{N_{\mathrm{G}}} P_{i,t}^{\mathrm{G}} + \sum_{k=1}^{N_{\mathrm{WE}}} (P_{k,t}^{\mathrm{W}} + P_{k,t}^{\mathrm{B,d}} - P_{k,t}^{\mathrm{B,c}}) = P_t^{\mathrm{L}} \tag{21}$$

$$-P_{l,\max} \le P_{l,t} \le P_{l,\max} \tag{22}$$

$$\sum_{i=1}^{N_{\mathrm{G}}} R_{i,t}^{\mathrm{G}} + \sum_{k=1}^{N_{\mathrm{WE}}} (R_{k,t}^{\mathrm{W}} + R_{k,t}^{\mathrm{B}}) \ge \varepsilon_{\mathrm{L}} P_t^{\mathrm{L}} + \varepsilon_{\mathrm{W}} \sum_{k=1}^{N_{\mathrm{WE}}} P_{k,t}^{\mathrm{forecast}} \tag{23}$$

where P_t^{L} is the forecasted load power at time t; $P_{k,t}^{\mathrm{B,d}}$ and $P_{k,t}^{\mathrm{B,c}}$ are the discharging power and charging power of ESS k at time t, respectively; $P_{l,t}$ is the active power transmitted by line l at time t; $P_{l,\max}$ is the maximum active power that can be transmitted by line l; and ε_{L} and ε_{W} are the scaling coefficients for the disturbances of system load and wind power, respectively.

3) Operational Constraints of Wind Farm

The operational constraints of wind farm include wind farm output power constraints, load shedding constraints, and PFR reserve constraint, as given in (24) and (25).

$$\begin{cases} 0 \le P_{k,t}^{\mathrm{W}} \le P_{k,t}^{\mathrm{forecast}} \\ P_{k,t}^{\mathrm{W}} = (1 - u_{k,t}) P_{k,t}^{\mathrm{forecast}} \\ 0 \le u_{k,t} \le u_{\max} \end{cases} \tag{24}$$

$$\begin{cases} P_{k,t,\max}^{\mathrm{W,L}} = P_{k,t}^{\mathrm{forecast}} k_{\mathrm{d}} (-\Delta f_{\mathrm{ss}}^*) \\ P_{k,t,\max}^{\mathrm{W,L}} \le u_{k,t} P_{k,t}^{\mathrm{forecast}} \\ P_{k,t,\max}^{\mathrm{W,L}} \le (u_{\max} - u_{k,t}) P_{k,t}^{\mathrm{forecast}} \\ R_{k,t}^{\mathrm{W}} \ge P_{k,t,\max}^{\mathrm{W,L}} \end{cases} \tag{25}$$

where $P_{k,t,\max}^{\mathrm{W,L}}$ is the amount of steady-state PFR power change of wind farm k at time t; $u_{k,t}$ is the level of load shedding for wind farm k at time t; and $u_{\max}$ is the maximum level of load shedding.

4) Operational Constraints of ESS

The operational constraints of ESS encompass several key factors, including charging/discharging state constraints (26), power capacity constraints, state of charge (SOC) constraints (27), and PFR reserve constraints (28).

$$\begin{cases} 0 \le B_{k,t}^{\mathrm{B,d}} + B_{k,t}^{\mathrm{B,c}} \le 1 \\ B_{k,t}^{\mathrm{B,d}} P_{k,\min}^{\mathrm{d}} \le P_{k,t}^{\mathrm{B,d}} \le B_{k,t}^{\mathrm{B,d}} P_{k,\max}^{\mathrm{d}} \\ B_{k,t}^{\mathrm{B,c}} P_{k,\min}^{\mathrm{c}} \le P_{k,t}^{\mathrm{B,c}} \le B_{k,t}^{\mathrm{B,c}} P_{k,\max}^{\mathrm{c}} \end{cases} \tag{26}$$

where $P_{k,\min}^{\mathrm{d}}$ and $P_{k,\max}^{\mathrm{d}}$ are the minimum and maximum discharging power of ESS k, respectively; $P_{k,\min}^{\mathrm{c}}$ and $P_{k,\max}^{\mathrm{c}}$ are the minimum and maximum charging power of ESS k, respectively; and $B_{k,t}^{\mathrm{B,d}}$ and $B_{k,t}^{\mathrm{B,c}}$ are the binary variables representing the discharging and charging states of ESS k at time t, respectively.

$$\begin{cases} SOC_{\min} \le SOC_{k,t} \le SOC_{\max} \\ SOC_{k,1} = SOC_{k,\mathrm{ini}} + \left(\eta_{k,\mathrm{c}} P_{k,1}^{\mathrm{B,c}} - \dfrac{P_{k,1}^{\mathrm{B,d}}}{\eta_{k,\mathrm{d}}} \right) \Delta t / S_s \\ SOC_{k,t} = SOC_{k,t-1} + \left(\eta_{k,\mathrm{c}} P_{k,t}^{\mathrm{B,c}} - \dfrac{P_{k,t}^{\mathrm{B,d}}}{\eta_{k,\mathrm{d}}} \right) \Delta t / S_s \quad t = 2, 3, \ldots, T \\ SOC_{k,T} = SOC_{k,\mathrm{ini}} \\ SOC_{\min} \le \dfrac{SOC_{k,t} - (P_{k,t}^{\mathrm{B,d}} + R_{k,t}^{\mathrm{B}}) / \eta_{k,\mathrm{d}}}{S_s} \le SOC_{\max} \\ SOC_{\min} \le \dfrac{SOC_{k,t} - (P_{k,t}^{\mathrm{B,d}} - R_{k,t}^{\mathrm{B}}) / \eta_{k,\mathrm{d}}}{S_s} \le SOC_{\max} \\ SOC_{\min} \le \dfrac{SOC_{k,t} + (P_{k,t}^{\mathrm{B,c}} + R_{k,t}^{\mathrm{B}}) \eta_{k,\mathrm{c}}}{S_s} \le SOC_{\max} \\ SOC_{\min} \le \dfrac{SOC_{k,t} + (P_{k,t}^{\mathrm{B,c}} - R_{k,t}^{\mathrm{B}}) \eta_{k,\mathrm{c}}}{S_s} \le SOC_{\max} \end{cases} \tag{27}$$

where $SOC_{k,t}$ is the SOC of ESS k at time t; $SOC_{\max}$ and $SOC_{\min}$ are the maximum and minimum values of SOC, respectively; $SOC_{k,\mathrm{ini}}$ is the initial SOC of ESS k; $\eta_{k,\mathrm{c}}$ and $\eta_{k,\mathrm{d}}$ are the charging and discharging efficiencies of ESS k, respectively; amd S_s is the capacity of ESS.

$$\begin{cases} P_{k,t,\max}^{\mathrm{B,L}} = \max(0, P_{k,\max}^{\mathrm{B}} k_{\mathrm{d}} - B_{k,t}^{\mathrm{WE,s}} P_{k,t}^{\mathrm{forecast}} k_{\mathrm{d}}) \cdot (-\Delta f_{\mathrm{ss}}^{*}) \\ P_{k,t}^{\mathrm{B,d}} + P_{k,t,\max}^{\mathrm{B,L}} \le P_{k,\max}^{\mathrm{d}} \\ -P_{k,t}^{\mathrm{B,c}} + P_{k,t,\max}^{\mathrm{B,L}} \le P_{k,\max}^{\mathrm{d}} \\ P_{k,t}^{\mathrm{B,d}} - P_{k,t,\max}^{\mathrm{B,L}} \ge -P_{k,\max}^{\mathrm{c}} \\ -P_{k,t}^{\mathrm{B,c}} - P_{k,t,\max}^{\mathrm{B,L}} \ge -P_{k,\max}^{\mathrm{c}} \\ R_{k,t}^{\mathrm{B}} \ge P_{k,t,\max}^{\mathrm{B,L}} \end{cases} \tag{28}$$

where $P_{k,t,\max}^{\mathrm{B,L}}$ is the amount of steady-state PFR power change of ESS k at time t.

C. Proposed FCUC Model

We integrate the derived frequency response indices with the UC model to construct the FCUC model. The frequency constraints include the maximum RoCoF constraints, steady-state frequency deviation constraints, and frequency nadir constraints.

$$\begin{cases} (11) \\ \text{s.t. } (17)\text{-}(28) \\ \quad -\Delta P_{\mathrm{LW}} \left[\sum_{k=1}^{N_{\mathrm{WE}}} \max(0, P_{k,\max}^{\mathrm{B}} k_{\mathrm{d}} - B_{k,t}^{\mathrm{WE,s}} P_{k,t}^{\mathrm{forecast}} k_{\mathrm{d}}) + \right. \\ \quad\quad \left. \sum_{i=1}^{N_{\mathrm{G}}} \frac{B_{i,t}^{\mathrm{G}} P_{\mathrm{N},i}^{\mathrm{G}}}{R_i} + \sum_{k=1}^{N_{\mathrm{WE}}} P_{k,t}^{\mathrm{forecast}} k_{\mathrm{d}} + k_{\mathrm{L}} P_{\mathrm{Ln},t} \right]^{-1} \ge \Delta f_{\mathrm{ss,lim}} \\ \quad \dfrac{\Delta P_{\mathrm{LW}}}{2 \sum_{i=1}^{N_{\mathrm{G}}} B_{i,t}^{\mathrm{G}} P_{\mathrm{N},i}^{\mathrm{G}} H_{\mathrm{G},i}} \le RoCoF_{\mathrm{lim}} \\ \quad \Delta f_{\mathrm{nadir},t} \ge \Delta f_{\mathrm{nadir,lim}} \end{cases} \tag{29}$$

where $RoCoF_{\mathrm{lim}}$ is the maximum RoCoF limit of system; $\Delta f_{\mathrm{ss,lim}}$ is the steady-state frequency deviation limit of system; $\Delta f_{\mathrm{nadir},t}$ is the frequency nadir at time t; and $\Delta f_{\mathrm{nadir,lim}}$ is the frequency nadir limit of system.

IV. Model-based Multi-directional Bilayer Solution Method

The conventional method for determining the frequency nadir involves applying the inverse Laplace transform to obtain the time-domain expression of the system frequency deviation. This expression is then used to calculate the frequency nadir. Although this method is suitable for low-order frequency response models, its direct application to highly nonlinear frequency response models presents challenges in accurately calculating the frequency nadir. As demonstrated in Fig. 2, the coordinated frequency control strategy among PFR resources necessitates a precise representation of its frequency regulation characteristics. To achieve this, it is imperative to consider the impact of the highly nonlinear limiting module.

To tackle the aforementioned issues, this study employs model simulation to obtain the frequency nadir. The use of the simulation model is essential to implement the frequency nadir constraint established in the FCUC model. Consequently, traditional commercial linear solvers are unsuitable for directly solving the proposed FCUC model. Therefore, this paper introduces a model-based multi-directional bilayer solution method, where the inner and outer layers are interconnected by optimized cuts.

The inner problem is the FCUC model without the frequency nadir constraint. Its optimization results determine the PFR capability of system. On the other hand, the outer layer is built upon the results of the inner layer with incorporating frequency nadir constraint. This constraint evaluates whether the system response capability adheres to the stipulated frequency nadir requirement. If the frequency nadir of the outer solution fails to satisfy the frequency nadir constraint, the optimized cuts are generated to ensure the PFR capability can be improved to meet the frequency nadir.

The frequency nadir is influenced by multiple parameters [8]. H_{G}, R, and $K_{\mathrm{G}}^{\mathrm{P}}$ are selected to create optimized cuts to ensure a higher frequency nadir from three directions. The effect of the frequency control strategy of WT-ESS on the frequency nadir is also considered. Given that the parallel control can utilize a greater number of PFR resources and results in a higher frequency nadir in comparison to serial control, it is incorporated into the construction of the optimized cut. This results in three parallel optimization problems, which are solved simultaneously to select the least expensive one as the optimal solution.

The specific steps of this solution method are outlined as follows.

1) Solve and optimize the inner problem to acquire the operational states of each unit, which are subsequently transferred to the outer simulation model.

2) Using the operational states of the units, simulate the frequency nadir of system for each time in the outer simulation model. If the frequency nadir exceeds the limiting value, generate the optimized cuts in the following forms:

$$\begin{cases} H_{\mathrm{G},t}^{\mathrm{sum}} = \sum_{i=1}^{N_{\mathrm{G}}} B_{i,t}^{\mathrm{G}} H_{\mathrm{G},i} + \sum_{k=1}^{N_{\mathrm{WE}}} (1 - B_{k,t}^{\mathrm{WE,s}}) \quad H_{\mathrm{G},t}^{\mathrm{cut}} > H_{\mathrm{G},t}^{\mathrm{sum}} \\ R_t^{-1,\mathrm{sum}} = \sum_{i=1}^{N_{\mathrm{G}}} B_{i,t}^{\mathrm{G}} R_i^{-1} + \sum_{k=1}^{N_{\mathrm{WE}}} (1 - B_{k,t}^{\mathrm{WE,s}}) \quad R_t^{-1,\mathrm{cut}} > R_t^{-1,\mathrm{sum}} \\ K_{\mathrm{G},t}^{\mathrm{P,sum}} = \sum_{i=1}^{N_{\mathrm{G}}} B_{i,t}^{\mathrm{G}} K_{\mathrm{G},i}^{\mathrm{P}} + \sum_{k=1}^{N_{\mathrm{WE}}} (1 - B_{k,t}^{\mathrm{WE,s}}) \quad K_{\mathrm{G},t}^{\mathrm{P,cut}} > K_{\mathrm{G},t}^{\mathrm{P,sum}} \end{cases} \tag{30}$$

where $H_{\mathrm{G},t}^{\mathrm{sum}}$, $R_t^{-1,\mathrm{sum}}$, and $K_{\mathrm{G},t}^{\mathrm{P,sum}}$ are the sum of the inertia time constant, reciprocal of the adjustment coefficient, and proportional coefficients for all TPUs at time t, respectively; and $H_{\mathrm{G},t}^{\mathrm{cut}}$, $R_t^{-1,\mathrm{cut}}$, and $K_{\mathrm{G},t}^{\mathrm{P,cut}}$ are the next generated optimized cuts in the three parallel tasks.

3) The generated optimized cut is then passed back to the inner problem, and the optimization process is rerun to obtain a new feasible solution. When the following condition is satisfied, the frequency response of system can be enhanced at this juncture.

$$\sum_{i=1}^{N_{\mathrm{G}}} B_{i,t}^{\mathrm{G}} + \sum_{k=1}^{N_{\mathrm{WE}}} (1 - B_{k,t}^{\mathrm{WE,s}}) \le N_{\mathrm{G}} + N_{\mathrm{WE}} \tag{31}$$

4) Using the optimized cut conditions, iteratively increase the frequency nadir elevation until the frequency nadir constraints are met all the time. If neither the frequency nadir constraint nor (31) is met, a scheduling result that maximizes compliance with the frequency nadir constraint will be generated.

V. Case Studies

A. Test System

The proposed FCUC model is verified using a modified IEEE 39-bus standard test system. The system includes 9 TPUs (G1-G9). One WT-ESS is connected to bus 39. The total load is 1500 MW. The parameters of the WT-ESS are detailed in Table I, where the parameters related to frequency regulation are taken from [14] and [30]. The parameters of TPUs are provided in Table II [25], where t_{st} is the start-up and shut-down time.

TABLE I
Parameters of WT-ESS

Parameter	Value	Parameter	Value
Installed capacity of wind farm (MW)	650	k_d (p.u)	20
SOC_{max}	0.9	k_i (p.u)	8
SOC_{min}	0.3	$T_{w,i}$ (s)	0.1
P^d_{max}, P^c_{max} (MW)	100, 100	$T_{w,d}$ (s)	3
P^d_{min}, P^c_{min} (MW)	10, 10	T_E (s)	0.3
Installed capacity of ESS (MWh)	400	u_{max}	0.2
η_c	0.95	C^B ($/MWh)	40
η_d	0.95	C^W ($/MWh)	200

TABLE II
Parameters of TPUs

TPU	P^G_{max} (MW)	P^G_{min} (MW)	t_{st} (hour)	R	a ($/MWh)	b ($/hour)	d ($)	K^P_G	K^I_G	H_G
G1	200	40	2	0.042	54.82	105.18	700	6	2.4	4.3
G2	200	40	2	0.043	55.95	103.96	600	6	2.3	4.3
G3	250	50	3	0.045	43.68	116.02	900	12	2.3	4.5
G4	250	50	3	0.045	43.08	117.41	800	10	2.2	4.5
G5	250	50	3	0.045	44.51	115.44	800	13	2.4	4.5
G6	300	60	4	0.048	37.12	122.62	1500	16	2.2	4.8
G7	300	60	4	0.048	37.36	122.27	1500	14	2.1	4.8
G8	300	60	4	0.048	35.96	123.57	1400	18	2.3	4.8
G9	350	70	5	0.050	32.14	127.42	1600	19	2.2	5.0

The base frequency of the system is established at 50 Hz, and the daily load power and the maximum forecasted power of wind farm are illustrated in Fig. 4.

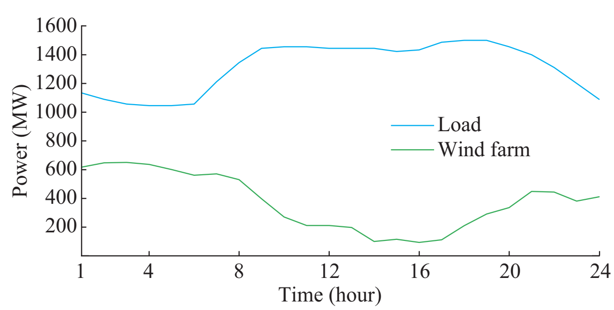

Fig. 4. Daily load power and the maximum forecasted power of wind farm.

The total disturbance to the system is 10% of the load power and wind power forecasts. The time resolution of unit commitment is set to be 1 hour. The reserve cost of TPU is determined as 15 $/MWh [8]. The adjustment coefficient of the load frequency is $k_L=1$ p.u.. Additionally, the safety requirement for frequency is defined as $RoCoF_{lim}=0.5$ Hz/s, $\Delta f_{nadir,lim}=49.5$ Hz, and $\Delta f_{ss,lim}=-0.2$ Hz.

Six models (M1-M6) are established for comparison to validate the proposed FCUC model.

1) M1: unit commitment model without considering frequency constraints.

2) M2: FCUC model only with TPU involved in PFR [21].

3) M3: FCUC model with TPU and WTs involved in PFR [8].

4) M4: FCUC model with TPU and WT-ESS involved in PFR, and the WT-ESS employs serial control.

5) M5: FCUC model with TPU and WT-ESS involved in PFR, and the WT-ESS employs parallel control.

6) M6 (the proposed one): FCUC model with TPU and WT-ESS involved in PFR, and the WT-ESS can switch between serial and parallel control.

The simulations are carried out on a computer with Intel Core i7 processor running at 4.7 GHz and 16 GB of memory. The optimal scheduling model is solved with the GUROBI package in MATLAB R2022b.

B. Results

The economic outcomes and dynamic frequency response indices of different models for the worst case in the scheduling cycle are presented in Table III. M1 exhibits the lowest operating cost. However, the maximum RoCoF, frequency nadir, and steady-state frequency deviation after the disturbance are 0.7722 Hz/s, 49.36 Hz, and −0.35 Hz, respectively, which violate the frequency constraints for all three frequency response indices.

TABLE III
Economic Outcomes and Dynamic Frequency Response Indices of Different Models

Model	Operating cost ($)	Extra cost (%)	$RoCoF_{max}$ (Hz/s)	Δf_{nadir} (Hz)	Δf_{ss} (Hz)
M1	880547.29	0	0.7722	49.36	−0.35
M2	1061244.65	20.52	0.4650	49.58	−0.20
M3	929474.84	5.56	0.4975	49.61	−0.20
M4	929486.35	5.56	0.4975	49.61	−0.20
M5	931334.26	5.77	0.4975	49.64	−0.19
M6	928606.29	5.46	0.4975	49.61	−0.20

1) *Effectiveness of Frequency Constraints in Scheduling*

The integration of frequency constraints into the FCUC model facilitates the adherence of the system dynamic frequency indices to safety regulations. However, this necessitates augmenting the PFR capability of the system, resulting in escalated operating costs. In M2, only TPU participates in PFR, which requires a higher number of TPUs to be turned on, and TPU will have more PFR reserves, which indirectly leads to an increase in wind power curtailment. Consequently, the operating cost after accounting for frequency constraints amounts to \$1061244.65 in M2, representing a 20.52% increase compared with that of M1.

In conclusion, while the integration of frequency constraints into the FCUC model is essential to ensure grid stability, it significantly increases operating costs due to the increased demands on PFR capacity, particularly when relying on TPUs exclusively.

2) Effectiveness of WT-ESS Under Different Frequency Control Strategies in Scheduling

Further consideration of the PFR capacity of WTs and ESS can diminish the requirement for PFR capacity from TPUs. This allows for a more flexible determination of TPU generation power, facilitating increased utilization of RESs.

In M3, where the ESS is not engaged in providing PFR capacity, the optimal scheduling result exhibits superior economic performance when compared with M4 and M5. This is attributed to the absence of PFR reserve costs for the ESS. However, neglecting the ESS during the PFR process could diminish the overall PFR effectiveness of the system. Figure 5 depicts the frequency response curve of the system at low wind speeds for M3-M5. Specifically, it is evident that when the ESS is excluded from PFR (M3), the frequency decrease is accelerated, resulting in a lower frequency nadir. Additionally, the dynamic frequency response performance of parallel control (M5) surpasses that of serial control (M4).

When assessing the capability of ESS to provide PFR capacity and considering the control strategy of WT-ESS, the cost of utilizing the WT-ESS under either a serial or parallel control alone amounts to \$929486.35 and \$931334.26, respectively. In M6, where the WT-ESS can seamlessly switch between serial and parallel control based on the system state, the cost is reduced to \$928606.29. This cost is lower than the cost when PFR is provided separately by the wind farms.

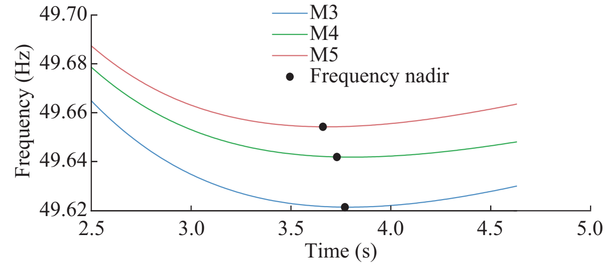

Fig. 5. Frequency response curve of system.

Compared with solely relying on TPU to participate in PFR, the consideration of the coordinated frequency control strategy of WT-ESS reduces the operating cost from \$1061244.65 to \$928606.29. Moreover, incorporating coordinated frequency control of WT-ESS reduces the operating cost of FCUC model by 12.5%.

Integrating PFR capacity of WT-ESS into frequency regulation offers economic and operational benefits. It reduces TPU reliance, enhances power generation flexibility, improves renewable energy utilization, and lowers system costs. WT-ESS adaptability between serial and parallel control optimizes the performance and cost-effectiveness.

3) Frequency Response Characteristics

Figure 6(a)-(f) illustrates the frequency response indices corresponding to each scheduling cycle under unexpected events and the on/off status of TPUs. As observed in Fig. 6(a), the maximum RoCoF is largely unmet in the majority of time periods with M1 when the system experiences an extreme power perturbation. This suggests that the system lacks sufficient inertia support to withstand rapid frequency changes adequately. When enforcing the frequency constraint, both M2 and M6 increase the overall inertia of the system by activating additional TPUs. This ensures compliance with the constraint throughout all periods.

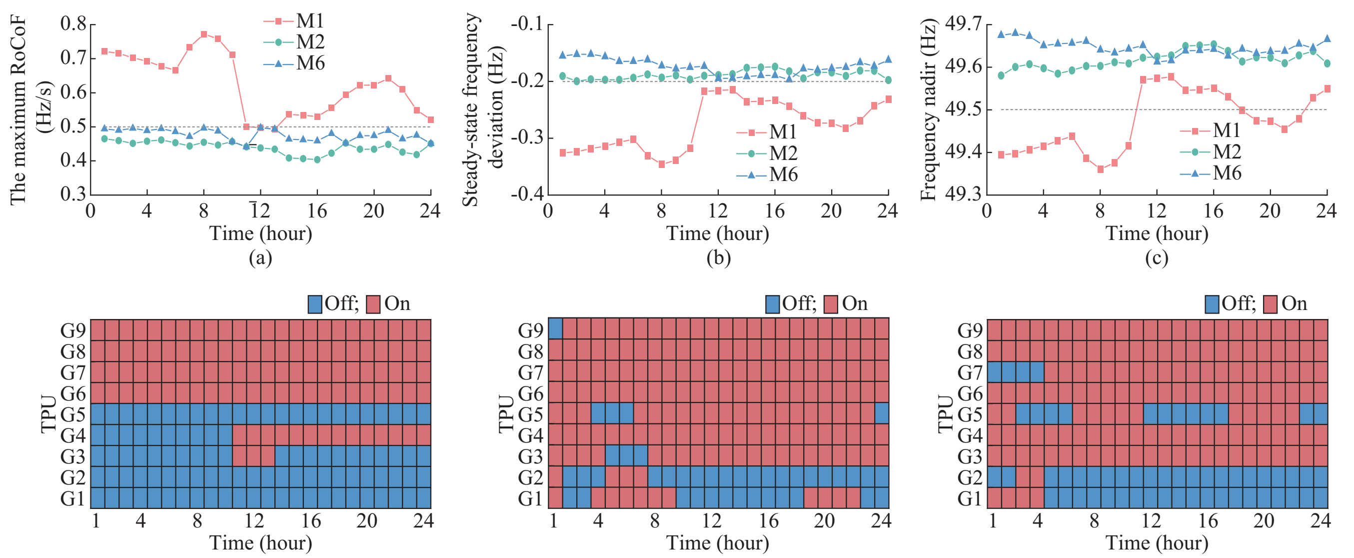

Fig. 6. Frequency response indices and on/off status of TPU. (a) The maximum RoCoF with M1, M2, and M6. (b) Steady-state frequency deviation with M1, M2, and M6. (c) Frequency nadir with M1, M2, and M6. (d) On/off status of TPU with M1. (e) On/off status of TPU with M2. (f) On/off status of TPU with M6.

As observed in Fig. 6(b), the system experiences an extreme power disturbance, resulting in a failure to meet the steady-state frequency deviation constraint during each period of M1. This suggests that the conventional unit commitment approach struggles to guarantee adequate PFR resources for the system. Conversely, both M2 and M6 ensure the compliance with the steady-state frequency deviation constraints all the time. Since M6 has more resources to participate in PFR than M2, the effect of M6 is better than that of M2 during most periods. Due to the increased availability of PFR resources, fewer TPUs need to be initiated while still satisfying the steady-state frequency deviation constraint. As a result, the effect of M6 may be lower than that of M2 during some periods.

As depicted in Fig. 6(c), during an extreme power disturbance, part of the time periods with M1 do not adhere to the frequency nadir constraint. Conversely, both M2 and M6 ensure compliance with the frequency nadir constraint across all periods. M6 generally outperforms M2 during most periods, while M2 exhibits superior performance in a few instances. This is due to similar reasons as analyzed in Fig. 6(b).

Neglecting the frequency constraints can indeed lead to the system being in an unsafe frequency state following an accident. In conjunction with Fig. 6(a) - (d), it is observed that the frequency dynamic indicator exhibits poor performance from 01:00 to 10:00 with M1. During 01:00-06:00, the generation from RESs is larger, making several TPUs shut down. Consequently, the overall PFR capability of the system becomes insufficient. During 07:00-10:00, there is a significant increase in electricity consumption. Despite this, RESs continue to provide a consistent output. The status of the TPU, whether on or off, remains unaltered. During this period, the system experiences heightened perturbations. However, the overall PFR capability of the system remains stable.

4) Reserved Situation

Figures 7-9 show the reserve required for each PFR resource with M4-M6, respectively, considering the participation of WT-ESS in PFR.

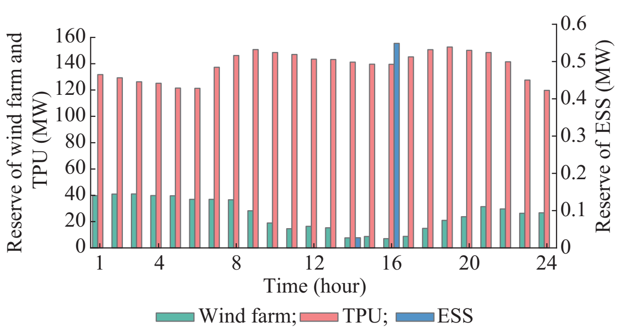

Fig. 7. Reserve required for each PFR resource with M4.

With M4, the WT-ESS employs a serial control, enabling the ESS to furnish reserve capacity for supporting system frequency during periods of low wind speed. This compensates for the diminished PFR capability resulting from the reduced wind power output. With M5, the WT-ESS is under the parallel control and the ESS can continuously provide reserve capacity to participate in the PFR. With M6, the WT-ESS can switch between serial and parallel control, which increases the system flexibility. When the demand for PFR diminishes, the reserve capacity provided by ESS is reduced to minimize costs. Conversely, when the demand for PFR is increased, the conversion to parallel control provides stronger PFR capability.

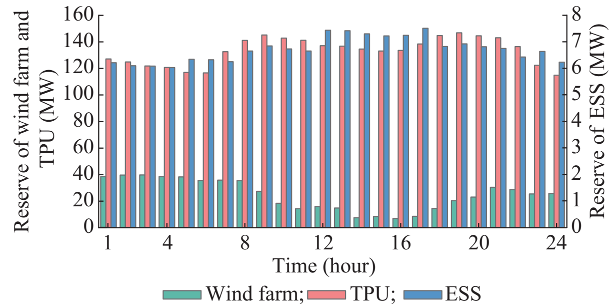

Fig. 8. Reserve required for each PFR resource with M5.

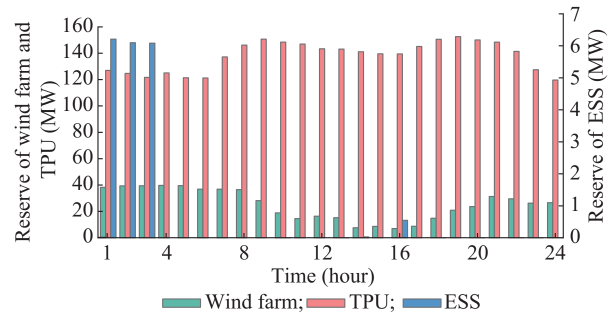

Fig. 9. Reserve required for each PFR resource with M6.

5) Effectiveness of Proposed Solution Method

The effectiveness of the proposed solution method is evaluated in terms of total execution time, solution time, and memory usage. All results are based on the average of five independent runs. The proposed solution method is employed to solve M1-M7, while the comparison solution method [24] is used for M8.

1) M7: FCUC model with TPU and WT-ESS involved in PFR, where only the frequency nadir constraint is considered among the frequency constraints. The proposed solution method is employed for the FCUC model.

2) M8: FCUC model with TPU and WT-ESS involved in PFR, where only the frequency nadir constraint is considered among the frequency constraints. The method of estimating the maximum perturbation that the system can withstand, i.e., the comparison method, is employed for the solution of the FCUC model.

To ensure that the scheduling results of M7 and M8 are only affected by the frequency nadir constraint, the steady-state frequency deviation constraint and the maximum RoCoF constraint are not considered in the FCUC model. Meanwhile, the penetration of wind power in the power system increases from 650 MW to 800 MW to enhance the comparison.

The results of M1-M6 in Table IV indicate that an increase in the number of factors considered leads to a corresponding rise in both solution time and memory usage. However, the proposed solution method exhibits acceptable performance in terms of the solution time, completing the unit commitment within a reasonable time frame. Additionally, its memory usage remains at a desirable level on the computer.

TABLE IV
TOTAL EXECUTION TIME, SOLUTION TIME, AND MEMORY USAGE WITH DIFFERENT MODELS

Model	Execution time (s)	Solution time (s)	Memory usage (MB)
M1	8.519	0.26	207.34
M2	17.428	5.33	233.71
M3	19.718	7.59	251.46
M4	19.698	7.37	276.44
M5	20.140	8.08	328.63
M6	22.830	10.93	341.78
M7	129.150	117.83	452.79
M8	1474.670	1455.75	439.36

To facilitate a comparative analysis of the solution time in the frequency nadir constraint, the frequency constraints in M7 and M8 are modified to include only the frequency nadir constraint, thereby expanding the search space of solver. Consequently, the solver requires more computing resources to traverse all possible solutions, resulting in longer solution time and higher memory usage of M7 compared with those of M1-M6. The solution time of M7 is shorter than that of M8. This advantage can be attributed to the introduction of a significant number of nonlinear terms in the scheduling model by M8, which subsequently escalates the solution time. In contrast, the proposed solution method addresses the frequency nadir constraint through simulation models, which are then integrated with the FCUC model via optimized cuts. The proposed solution method reduces the need for introducing nonlinear terms and consequently decreases solution time. Regarding memory usage, while the use of an external Simulink model slightly increases the memory usage of M7 compared with that of M8, the increase remains within acceptable limits.

As shown in Table V and Figs. 10-13, M7 utilizes fewer PFR resources to meet the frequency nadir constraints during most time periods compared with M8. This demonstrates that M7 can more accurately assess the PFR capability of the system and accurately reflect the PFR characteristics of the complex model. It reduces the redundancy of PFR resources and decreases operating costs.

TABLE V
OPERATING COST WITH M7 AND M8

Model	Operating cost ($)
M7	821283.74
M8	824036.71

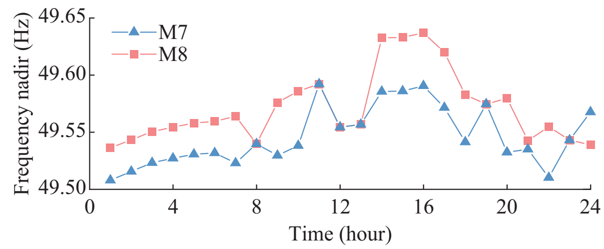

Fig. 10. Frequency nadir with M7 and M8.

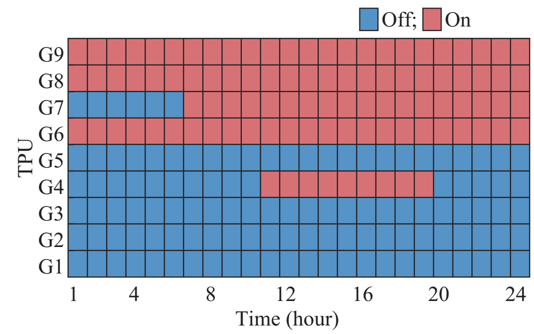

Fig. 11. On/off status of TPU with M7.

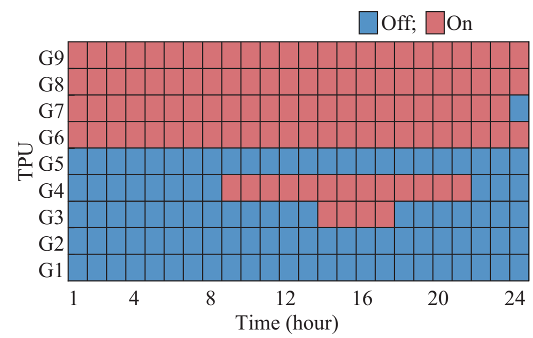

Fig. 12. On/off status of TPU with M8.

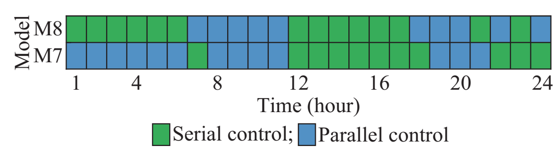

Fig. 13. Control strategy of WT-ESS.

VI. CONCLUSION

The frequency control strategy of WT-ESS plays a crucial role in ensuring frequency security in power systems with high renewable energy penetration. This study develops an FCUC model considering the coordinated frequency control strategy of the WT-ESS. By modeling the WT-ESS and integrating it into the FCUC model with considering its operating state and PFR capabilities under both serial control and parallel control. The proposed solution method effectively addresses highly nonlinear FCUC challenges. The numerical results validate the effectiveness of the proposed FCUC model and highlight several key findings.

1) Adjusting the operating state of TPU and considering the frequency control strategy of WT-ESS enable the frequency safety at the lowest cost. Incorporating coordinated

frequency control strategy of WT-ESS reduces the operating cost of FCUC model by 12.5%.

2) Flexibly adjusting the frequency control strategy of WT-ESS ensures sufficient PFR capabilities during each scheduling period, thereby keeping the frequency response indices within the specified range during emergencies.

3) The proposed solution method effectively constrains the three frequency indicators within their respective safe ranges for each time period, enhancing the system frequency security level.

In future research, we will investigate distributed control strategies for frequency stability in multi-microgrid systems, aiming to improve adaptability to various energy inputs. Additionally, we plan to consider the sizing and placement of ESS as optimization variables to assess their impact on power system frequency stability.

References

[1] Y. Li, D. W. Gao, W. Gao *et al*., "Double-mode energy management for multi-energy system via distributed dynamic event-triggered Newton-Raphson algorithm," *IEEE Transactions on Smart Grid*, vol. 11, no. 6, pp. 5339-5356, Nov. 2020.

[2] L. Liu, G. Yang, and S. Wasly, "Distributed predefined-time dual-mode energy management for a microgrid over event-triggered communication," *IEEE Transactions on Industrial Informatics*, vol. 20, no. 3, pp. 3295-3305, Mar. 2024.

[3] Y. Li, S. Lan, M. Ryberg *et al*., "A quantitative roadmap for China towards carbon neutrality in 2060 using methanol and ammonia as energy carriers," *iScience*, vol. 24, no. 6, p. 102513, Jun. 2021.

[4] Q. Sun, B. Huang, D. Li *et al*., "Optimal placement of energy storage devices in microgrids via structure preserving energy function," *IEEE Transactions on Industrial Informatics*, vol. 12, no. 3, pp. 1166-1179, Jun. 2016.

[5] S. Homan, N. M. Dowell, and S. Brown, "Grid frequency volatility in future low inertia scenarios: challenges and mitigation options," *Applied Energy*, vol. 290, p. 116723, May 2021.

[6] Q. Sun, Y. Zhang, H. He *et al*., "A novel energy function-based stability evaluation and nonlinear control approach for Energy Internet," *IEEE Transactions on Smart Grid*, vol. 8, no. 3, pp. 1195-1210, May 2017.

[7] J. F. Restrepo and F. D. Galiana, "Unit commitment with primary frequency regulation constraints," *IEEE Transactions on Power Systems*, vol. 20, no. 4, pp. 1836-1842, Nov. 2005.

[8] Z. Zhang, M. Zhou, Z. Wu *et al*., "A frequency security constrained scheduling approach considering wind farm providing frequency support and reserve," *IEEE Transactions on Sustainable Energy*, vol. 13, no. 2, pp. 1086-1100, Apr. 2022.

[9] Q. Zhang, J. Xie, X. Pan *et al*., "A short-term optimal scheduling model for wind-solar-hydro-thermal complementary generation system considering dynamic frequency response," *IEEE Access*, vol. 9, pp. 142768-142781, Oct. 2021.

[10] J. Li, Y. Qiao, Z. Lu *et al*., "Integrated frequency-constrained scheduling considering coordination of frequency regulation capabilities from multi-source converters," *Journal of Modern Power Systems and Clean Energy*, vol. 12, no. 1, pp. 261-274, Jan. 2024.

[11] C. Zhang, L. Liu, H. Cheng *et al*., "Frequency-constrained co-planning of generation and energy storage with high-penetration renewable energy," *Journal of Modern Power Systems and Clean Energy*, vol. 9, no. 4, pp. 760-775, Jul. 2021.

[12] G. Ramtharan, N. Jenkins, and J. B. Ekanayake, "Frequency support from doubly fed induction generator wind turbines," *IET Renewable Power Generation*, vol. 1, no. 1, pp. 3-9, Mar. 2007.

[13] Y. Tan, K. M. Muttaqi, P. Ciufo *et al*., "Enhanced frequency regulation using multilevel energy storage in remote area power supply systems," *IEEE Transactions on Power Systems*, vol. 34, no. 1, pp. 163-170, Jan. 2019.

[14] C. Li, Z. Zhang, J. Li *et al*., "Design of control strategy and effect evaluation for primary frequency regulation of wind storage system," *Frontiers in Energy Research*, vol. 9, p. 739439, Sept. 2021.

[15] L. Miao, J. Wen, H. Xie *et al*., "Coordinated control strategy of wind turbine generator and energy storage equipment for frequency support," *IEEE Transactions on Industry Applications*, vol. 51, no. 4, pp. 2732-2742, Jul. 2015.

[16] Z. Wu, D. W. Gao, H. Zhang *et al*., "Coordinated control strategy of battery energy storage system and PMSG-WTG to enhance system frequency regulation capability," *IEEE Transactions on Sustainable Energy*, vol. 8, no. 3, pp. 1330-1343, Jul. 2017.

[17] J. Kim, E. Muljadi, V. Gevorgian *et al*., "Dynamic capabilities of an energy storage-embedded DFIG system," *IEEE Transactions on Industry Applications*, vol. 55, no. 4, pp. 4124-4134, Jul. 2019.

[18] G. He, Q. Chen, C. Kang *et al*., "Cooperation of wind power and battery storage to provide frequency regulation in power markets," *IEEE Transactions on Power Systems*, vol. 32, no. 5, pp. 3559-3568, Sept. 2017.

[19] L. Liu, W. Li, Y. Ba *et al*., "An analytical model for frequency nadir prediction following a major disturbance," *IEEE Transactions on Power Systems*, vol. 35, no. 4, pp. 2527-2536, Jul. 2020.

[20] P. M. Anderson and M. Mirheydar, "A low-order system frequency response model," *IEEE Transactions on Power Systems*, vol. 5, no. 3, pp. 720-729, Aug. 1990.

[21] Q. Shi, F. Li, and H. Cui, "Analytical method to aggregate multi-machine SFR model with applications in power system dynamic studies," *IEEE Transactions on Power Systems*, vol. 33, no. 6, pp. 6355-6367, Nov. 2018.

[22] Z. Zhang, E. Du, F. Teng *et al*., "Modeling frequency dynamics in unit commitment with a high share of renewable energy," *IEEE Transactions on Power Systems*, vol. 35, no. 6, pp. 4383-4395, Nov. 2020.

[23] I. Egido, F. Fernandez-Bernal, P. Centeno *et al*., "Maximum frequency deviation calculation in small isolated power systems," *IEEE Transactions on Power Systems*, vol. 24, no. 4, pp. 1731-1738, Nov. 2009.

[24] Y. Zhang, Q. Guo, Y. Zhou *et al*., "Frequency-constrained unit commitment for power systems with high renewable energy penetration," *International Journal of Electrical Power & Energy Systems*, vol. 153, p. 109274, Nov. 2023.

[25] H. Ahmadi and H. Ghasemi, "Security-constrained unit commitment with linearized system frequency limit constraints," *IEEE Transactions on Power Systems*, vol. 29, no. 4, pp. 1536-1545, Jul. 2014.

[26] M. Paturet, U. Markovic, S. Delikaraoglou *et al*., "Stochastic unit commitment in low-inertia grids," *IEEE Transactions on Power Systems*, vol. 35, no. 5, pp. 3448-3458, Sept. 2020.

[27] Y. Fang, E. Du, H. Jiang *et al*., "Unit commitment with concentrating solar power considering operational risk and frequency dynamic constraints," *CSEE Journal of Power and Energy Systems*, doi: 10.17775/CSEEJPES.2022.06770

[28] M. Javadi, Y. Gong, and C. Y. Chung, "Frequency stability constrained microgrid scheduling considering seamless islanding," *IEEE Transactions on Power Systems*, vol. 37, no. 1, pp. 306-316, Jan. 2022.

[29] G. Kou, P. Markham, S. Hadley *et al*., "Impact of governor deadband on frequency response of the U. S. eastern interconnection," *IEEE Transactions on Smart Grid*, vol. 7, no. 3, pp. 1368-1377, May 2016.

[30] J. Dong, F. Gao, X. Guan *et al*., "Storage-reserve sizing with qualified reliability for connected high renewable penetration micro-grid," *IEEE Transactions on Sustainable Energy*, vol. 7, no. 2, pp. 732-743, Apr. 2016.

Hui Hwang Goh received the B.Eng., M.Eng., and Ph.D. degrees from the University Technology Malaysia, Johor Bahru, Johor, Malaysia, in 1998, 2002, and 2007, respectively. He is currently a Professor with Guangxi Key Laboratory of Power System Optimization and Energy Technology, Guangxi University, Nanning, China. His research interests include embedded power generation modeling and simulation, power quality, renewable energy, and dynamic equivalent.

Yuxin Ou received the B.S. degree in electrical engineering and automation from Guangxi University, Nanning, China, in 2022. He is currently working toward the M.S. degree with Guangxi Key Laboratory of Power System Optimization and Energy Technology, Guangxi University. His research interest includes frequency-constrained unit commitment.

Wei Dai received the B.S. degree in electric power system and automation from Yanshan University, Qinhuangdao, China, in 2014, and the Ph.D. degree in electrical engineering from Chongqing University, Chongqing, China, in 2018. He currently works as an Associate Professor with Guangxi University, Nanning, China. His research interests include optimal scheduling of novel power system, power system risk assessment and planning, coordinated operation of integrated energy system, and artificial intelligence.

Hui Liu received the M.S. and Ph.D. degrees in electrical engineering from the College of Electrical Engineering, Guangxi University, Nanning, China, in 2004 and 2007, respectively. He was a Postdoctoral Fellow with Tsinghua University, Beijing, China, from 2011 to 2013, and a Faculty Member with Jiangsu University, Zhenjiang, China, from 2007 to 2016. From 2014 to 2015, he visited the Energy Systems Division, Argonne National Laboratory, Argonne, USA. In 2016, he joined the College of Electrical Engineering, Guangxi University, where he is currently a Professor. He is an Associate Editor for the IEEE Transactions on Smart Grid and IET Generation, Transmission & Distribution. His research interests include power system optimization, power system stability and control, electric vehicle, integrated energy system, and demand response.

Tonni Agustiono Kurniawan received the Ph. D. degree from the Hong Kong Polytechnic University, Hong Kong, China. He is an Associate Professor with Xiamen University, Xiamen, China. Prior to joining the University, he was a Scholar with United Nations University, Tokyo, Japan. Since 2011, the Institute for Scientific Information-Thompson Reuters has identified him among the top 1% of researchers in the field of engineering according to the Essential Science Indicators of Web of Knowledge. His research interests include wastewater treatment and water purification.

Jun Xu received the B.S. degree in electrical engineering and automation from the Huazhong University of Science and Technology, Wuhan, China, in 2020, and the M.S. degree in electrical engineering from Guangxi University, Nanning, China, in 2024. His research interests include power system frequency regulation and renewable energy.